AIAA 82-4128

Precision Release and Aim of Payloads Launched by Lunar Mass-Driver

T.A. Heppenheimer*
Center for Space Science, Fountain Valley, Calif.
David J. Ross†
Phoenix Engineering, Inc., Palo Alto, Calif.
and
Eric C. Hannah‡
Hewlett-Packard Research Laboratories, Palo Alto, Calif.

Payloads launched by lunar mass-driver do not incorporate onboard midcourse correction, and their trajectories must accurately attain a specified launch state. We offer an integrated mass-driver launch system employing several novel features. We discuss payload containment and release, proposing a means for low-dispersion release. We propose "electromagnetic fins" for passive eddy-current damping of oscillations of the payload carriers (buckets). We consider the magnetic interaction of payload and bucket during payload separation and release, as a source of launch errors. We propose a novel optical scanner and note its use in a sequence which determines position errors of a payload center of mass. Finally, we indicate applications of basic mass-driver technology to the magnetic correction of payload trajectories, discussing adjustment of both transverse and longitudinal velocity components. It appears that the largest residual error source is a transverse velocity component ~0.003 cm/s, which for a mass-catcher near the L_2 libration point implies a circular error probable of diameter ~3 m.

I. Introduction

In recent years the mass-driver has received attention as a means for transportation of lunar resources. The principal subject for attention has been the mass-driver proper: an electromagnetic accelerator employing dynamic magnetic levitation and the linear synchronous motor (LSM), which accelerates payloads aboard payload carriers ("buckets"). However, a lunar launch system in addition requires means to reduce the dispersion of launched payloads, which fly ballistically to a mass-catcher without onboard guidance. Hence the mass-driver must achieve low launch dispersion, and in addition must be integrated as a system with auxiliary equipment which detects and corrects residual dispersions.

Some elements of this problem have been treated. Chilton et al.[1] have suggested elements of a technique for optical tracking and magnetic correction of bucket flight paths, followed by electrostatic adjustment of payload trajectories. Malzbender[2] has proposed an optical scanner employing a rapidly rotating mirror. Heppenheimer[3] has considered passive mechanical damping as a means of reducing postlaunch dispersions and, by presenting the concept of achromatic trajectories,[4] has eased the problem of control of the launch velocity magnitude. The present authors[5] have studied electrostatic correction of payload trajectories.

Figure 1 defines the basic problem in terms of dispersion coefficients.[4] A payload at release has velocity components V_T, V_N, V_Z as indicated. In addition there are component errors $\Delta V_T, \Delta V_N, \Delta V_Z$ in cm/s. Associated with these are the displacement errors at the target, taken here as the L_2 (translunar) libration point, some 64,000 km behind the moon. The linear displacement errors are $\Delta z = C_{VZ}\Delta V_Z$, $\Delta y = C_{VN}\Delta V_N + C_{VT}\Delta V_T$. However, by using achromatic trajectories one has $C_{VT}=0$ and hence one writes $\Delta y = C_{VN}\Delta V_N + C_{VT2}\Delta V_T^2$. One thus may avoid the need for a tight bound on ΔV_T; $\Delta V_T > 1$ cm/s gives $\Delta y \sim 1$ m. However, one still must control $\Delta V_N, \Delta V_Z$; per meter of allowed Δy, Δz, one requires $\Delta V_Z = C_{VZ}^{-1}$ cm/s, $\Delta V_N = C_{VN}^{-1}$ cm/s. The basic problem then is the routine achievement of low values of ΔV_N, ΔV_Z.

Figure 2 outlines the character of the solution approach treated here. This block diagram defines the principal functions of the mass-driver subsystems:

1) acceleration—the mass-driver proper (an LSM); 2) passive magnetic damping—eddy-current damping of bucket oscillations acquired during acceleration; 3) separation and snapout—separation of payload from bucket, and rapid removal of bucket from the payload trajectory; and 4) downrange correction—optical detection and electrostatic or magnetic correction of residual values of $\Delta V_N, \Delta V_Z, \Delta V_T$.

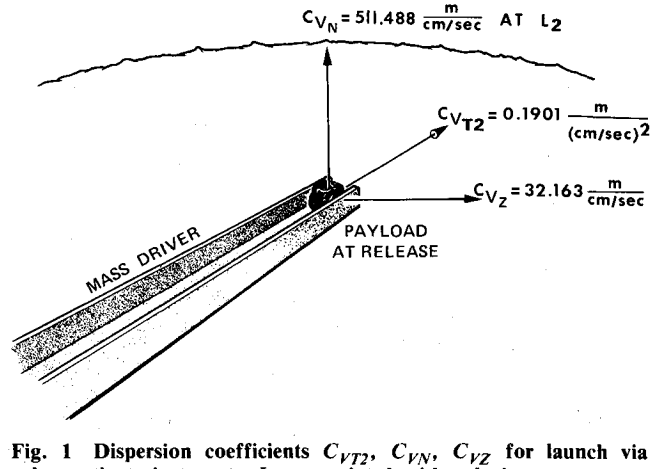

Fig. 1 Dispersion coefficients C_{VT2}, C_{VN}, C_{VZ} for launch via achromatic trajectory to L_2, associated with velocity components $\Delta V_T, \Delta V_N, \Delta V_Z$.

Received Dec. 16, 1980; revision received Nov. 16, 1981. Copyright © 1982 by T.A. Heppenheimer. Published by the American Institute of Aeronautics and Astronautics, Inc., with permission.

*President. Associate Fellow AIAA.
†President.
‡Member of the Technical Staff.

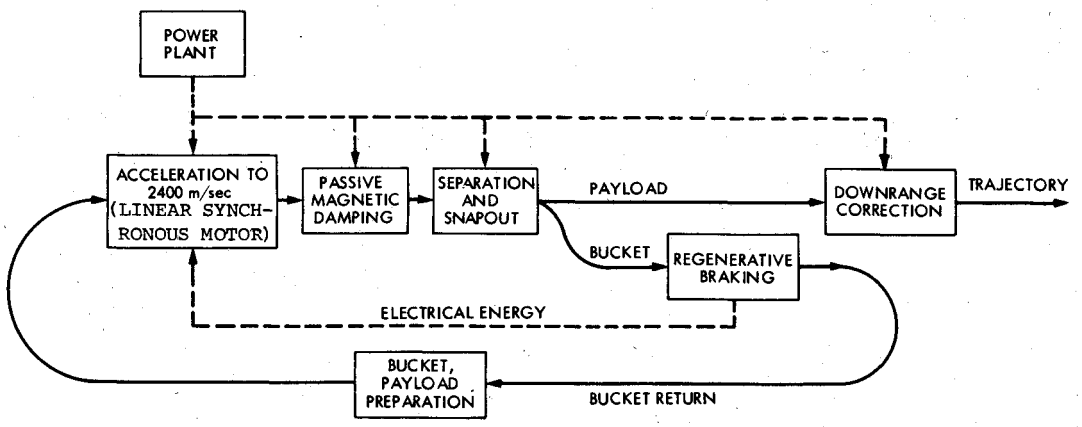

Fig. 2 Block diagram of lunar mass-driver launch system.

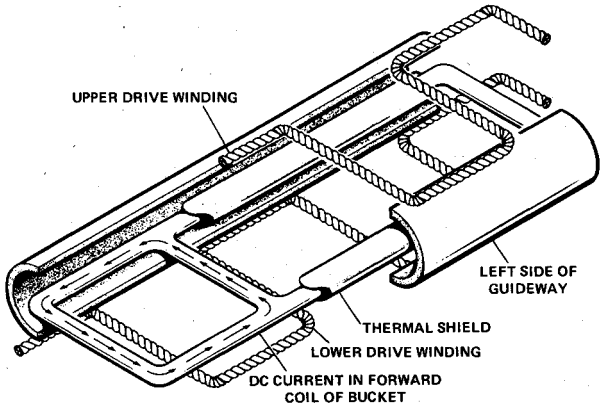

Fig. 3 Planar mass-driver geometry (after Ref. 6).

Each function will now be treated in turn. The functions of "regenerative braking" (bucket deceleration by LSM with energy recovery) and "bucket, payload preparation" are regarded as ancillary and will be referred to in passing.

II. Acceleration

Figure 3 illustrates a reference mass-driver geometry, derived from the experimental "Magneplane" concept[9] for high-speed ground transport. Only one of three phases of drive winding is shown. This geometry inherently controls roll and in addition lends itself to means for separating payload from bucket which provide that the principal sources of dispersion are in the z direction. This feature is desirable since $C_{VZ} \ll C_{VN}$ (Fig. 1). Figure 4 then illustrates a reference bucket concept. The superconducting coil configuration is taken from Ref. 6; Fig. 4b shows the current geometry as an oriented pair of square loops in the x-y plane. Here $u = 25$ cm.

The new feature of Fig. 4a is the payload housing and release system. A payload is ellipsoidal and is housed within two tightly fitting hemiellipsoidal shells. The rear shell is strongly braced. The front shell can telescope forward with a damped motion, but during bucket acceleration is pressed tightly backward. The use of this system in payload separation will be discussed separately.

III. Passive Damping

Bucket suspension during acceleration is via electromagnetic flight, which characteristically sustains undamped oscillations at frequencies $\omega > 100$ rad/s.[6] Such oscillations may be driven by guideway misalignments; they then have amplitude X limited by guideway clearance. Typically $X \sim 1$ cm; hence one anticipates $\Delta V_N, \Delta V_Z \sim \omega X > 1$

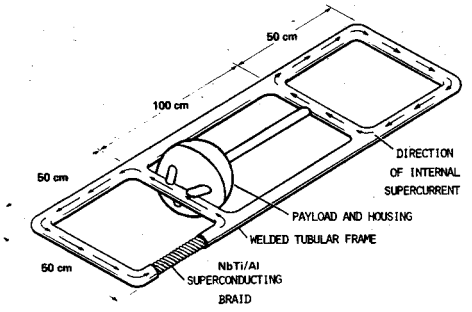

Fig. 4a Bucket, showing superconducting coils and payload housing.

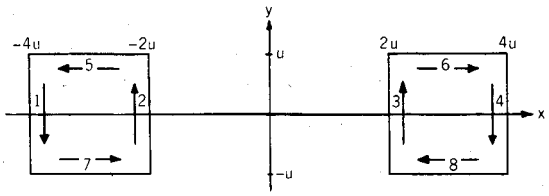

Fig. 4b Geometry of currents in the super conductors of Fig. 4a; z-axis is out of plane.

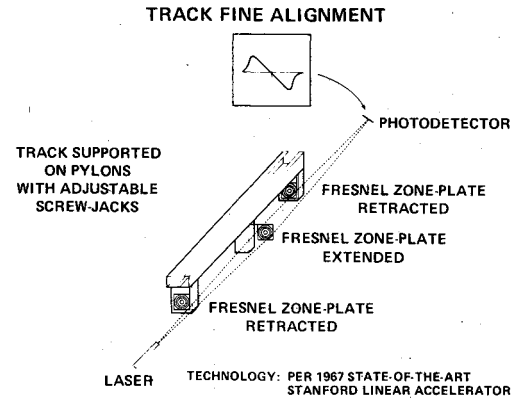

Fig. 5 Optical fine-alignment system for the guideway.

m/s. One thus must provide an accurately aligned length of guideway subsequent to acceleration, and must further provide means for damping the pre-existing oscillations.

Figure 5 indicates a method for fine alignment of the guideway, or of a supporting girder. This method is used in fine alignment of the Stanford Linear Accelerator.[10] A straight line is defined between a helium-neon laser and a photodetector. At each guideway support a remotely actuated

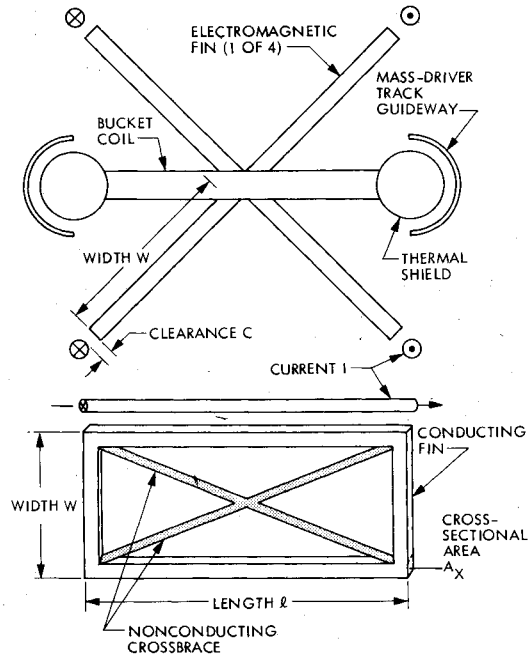

Fig. 6 Cross-sectional end view of the bucket of Fig. 4a within the guideway, and fitted with four cruciform electromagnetic fins. One such fin and its adjacent current-carrying conductor shown in side view.

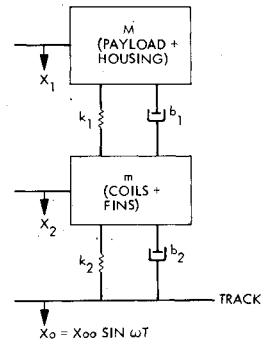

Fig. 7a Mathematical model for bucket with payload, oscillating within the guideway.

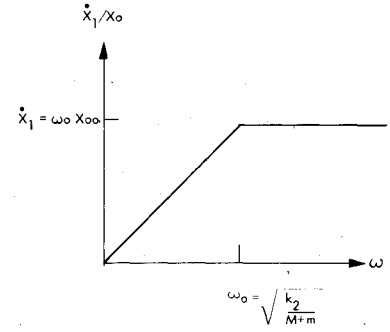

Fig. 7b Schematic Bode plot for rigid coupling between *m* and *M*.

hinge supports a target. To check alignment at a desired point, the target is extended into the light beam; the target is a Fresnel lens with the correct focal length so that an image of the light is formed on the plane of the detector. The detector then scans this image in both the vertical and horizontal directions to determine the displacement of the lens from the reference line.

The detector incorporates an electromechanical scanning system which generates the derivative of the spot intensity as a function of detector position. The center of the spot is defined as the point where the derivative is zero; the steep derivative line intersecting the axis gives an unambiguous determination. The sensitivity of determining the position of any target is $\pm 2.5 \times 10^{-4}$ cm. The resolution of shift of any of the pillar-mounted guideway support points is $\pm 2.5 \times 10^{-3}$ cm.

Damping of pre-existing oscillations is achievable using eddy-current damping. In Fig. 6, the bucket of Fig. 4, shown in an end view in cross section, is fitted with four cruciform "electromagnetic fins." Each fin is a rectangular conducting frame of length l, width W, cross-sectional area A_x, oriented parallel to the track. Each fin interacts with the magnetic field of a long conductor carrying current I. Transverse bucket oscillations thus induce eddy currents in the fins, which by Lenz' law act to oppose and hence to damp these oscillations.

Let a bucket oscillate along the diagonal joining two such conductors; its transverse velocity is $\dot{X}_2$. The eddy-current force acting to oppose this motion has magnitude

$$F = -(l^2/R)(\Delta B)^2 \dot{X}_2 \quad \text{N} \tag{1}$$

where R is fin resistance in ohms and ΔB is the change in magnetic induction due to the conductors carrying current I, across the fin width. In Fig. 6, the fin crosspieces of length W make no contribution to ΔB. The nearer of the lengthwise fin elements has clearance C from its adjacent conductor, $C \ll W$. Hence we regard each fin as acted upon only by the nearest conductor; then

$$\Delta B = 2 \cdot \frac{\mu_0 I}{2\pi} \left(\frac{1}{C} - \frac{1}{C+W} \right) \quad \text{T} \tag{2}$$

μ_0 the permeability constant, is $4\pi \times 10^{-7}$ in mks units, and both fins parallel to $\dot{X}_2$ are active. More generally one writes $\dot{X}_2$ for $\dot{X}_2$, $\dot{X}_2$ being a transverse velocity vector of general orientation; then Eqs. (1) and (2) hold with F replaced by $\boldsymbol{F}$. Now let b_2 be the damping coefficient; we have

$$F = -b_2 \dot{X}_2 = -\frac{2}{R} \left(\frac{\mu_0 I l W}{2\pi C(C+W)} \right)^2 \dot{X}_2 \quad \text{N} \tag{3}$$

where R is given as

$$R = 2\rho_{\text{fin}} (l+W)/A_x \quad \Omega \tag{4}$$

and ρ_{fin} is the resistivity of the fin material in ohm-meters.

Figure 7 then presents a model for the damped oscillations. In Fig. 4a the payload and housing may be regarded as nonrigidly coupled to the rest of the bucket. In Fig. 7a the payload and housing have mass M, and are coupled via spring constant k_1 and damping coefficient b_1 to the bucket coils and fins of Fig. 6, having mass m. Here X_0 is track or guideway displacement; with $V_T = 2400$ m/s, $X_0 = X_{00} \sin \omega t$, where X_{00} is guideway misalignment amplitude, ω is forced oscillation frequency, t is time. Also m and the guideway are coupled through spring constant k_2, resulting from magnetic repulsion of bucket coils from the guideway[6]:

$$k_2 = \frac{9}{8} \frac{\mu_0 i^2}{2\pi} \frac{l_c}{S^2 - X_2^2} \quad \text{N/m} \tag{5}$$

where i is current in the bucket coils, S is coil-to-guideway distance, and l_c is length of bucket coil conductor facing the guideway surface. In Fig. 4, $l_c = 2$ m for out-of-plane oscillations and $l_c = 1$ m for lateral oscillations.

From Fig. 7a one has the Laplace transform of the differential equations relating displacements X_1, X_2 to

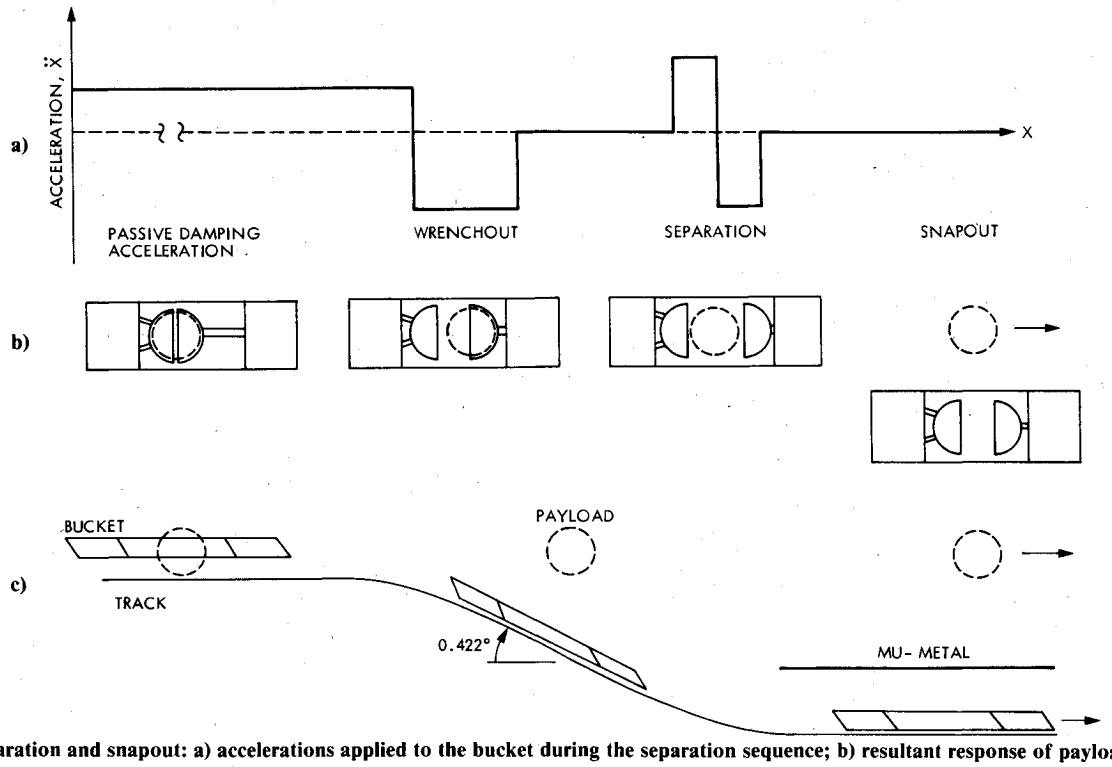

Fig. 8 Separation and snapout: a) accelerations applied to the bucket during the separation sequence; b) resultant response of payload within its housing; c) snapout maneuver.

misalignment X_0:

$$\begin{pmatrix} Ms^2+b_1s+k_1 & -(b_1s+k_1) \\ -(b_1s+k_1) & ms^2+(b_1+b_2)s+(k_2+k_2) \end{pmatrix}\begin{pmatrix} X_1 \\ X_2 \end{pmatrix}=\begin{pmatrix} 0 \\ (b_2s+k_2)X_0 \end{pmatrix} \tag{6}$$

where $s=\mathrm{d}/\mathrm{d}t$. Taking $s=\omega\sqrt{-1}$ and inverting, there is the frequency response $\dot{X}_1/X_0$ following decay of transients, where $\dot{X}_1$ is ΔV_N or ΔV_Z:

$$\frac{\dot{X}_1}{X_0}=\frac{s[1+(b_1/k_1)s]\,[1+(b_2/k_2)s]}{1+\left[\frac{b_1}{k_1}+\frac{b_2}{k_2}\right]s+\left[\frac{M+m}{k_2}+\frac{M}{k_1}+\frac{b_1b_2}{k_1k_2}\right]s^2+\left[\frac{b_1(M+m)+b_2M}{k_1k_2}\right]s^3+\frac{Mm}{k_1k_2}s^4} \tag{7}$$

k_1 acts to introduce vibrational isolation and to reduce $\dot{X}_1$. For $k_1 \gg k_2$, e.g., a nearly rigid coupling between M and m, this isolation is ineffective and Eq. (7) becomes

$$\frac{\dot{X}_1}{X_0}=\frac{s[1+(2\zeta/\omega_0)s]}{1+(2\zeta/\omega_0)s+(1/\omega_0^2)s^2} \tag{8}$$

where $\omega_0^2=k_2/(m+M)$ and $\zeta=\tfrac{1}{2}b_2[k_2(M+m)]^{-\frac{1}{2}}$. Figure 7b then approximates the Bode plot for Eq. (8); maximum $\dot{X}_1=\omega_0X_{00}$ occurs for $\omega \geq \omega_0$.

For example, in Fig. 6, let the fins be of aluminum with $l=1$ m, $W=32$ cm, $A_x=4$ cm^2, $C=4$ cm; with density $\rho_{kg}=2.7$ g/cm^3, the fins have mass 11.4 kg. Payload mass is 20 kg (Ref. 6); hence payload radius is $a=13$ cm for density 2.2 g/cm^3, a typical value for lunar soil. If the payload housing is of 0.5-cm aluminum then this housing plus braces are some 5 kg; hence we take $M=25$ kg. From Ref. 6 the bucket coils plus associated structure are 17 kg; hence $m=28.4$ kg.

In Eq. (5) $i=10^5$ A and $S=6$ cm.[6] Hence $k_2=12.5\times10^3$ N/cm for out-of-plane oscillations and $k_2=6.25\times10^3$ N/cm for lateral oscillations, with l_c as noted. Then $\omega_0=153$ and 108.2 s^{-1}, respectively; $\dot{X}_1=0.38$ and 0.27 cm/s, respectively. This confirms the orientation of Fig. 4b, for which $\dot{X}_1=\Delta V_Z$ for out-of-plane oscillations (in the z direction) and $\dot{X}_1=\Delta V_N$ for lateral (y direction) oscillations.

In Eq. (4), $\rho_{fin}=2.824\times10^{-8}$ Ω-m; hence $R=1.86\times10^{-4}$ Ω and, from Eq. (3), $b_2=2.12\times10^{-7}\,I^2$ N-s/m. Let $\zeta=0.5$ for ΔV_Z and $\zeta=0.707$ for ΔV_N; then $I=3.49\times10^5$ A. Hence the long conductors of Fig. 6 must be superconducting. If their technology follows that of Fig. 4, they carry an experimentally verified current density of 25,000 A/cm^2,[6] and have radius 2.11 cm. We note in passing that higher current densities may be possible.[11] Hence with $V_T=2400$ m/s the distance for ΔV_Z and ΔV_N to diminish by a factor 2.718 is $V_T/(\omega_0(1-\zeta^2)^{\frac{1}{2}})$ which is respectively 18.1 and 31.4 m. A 200-m fine aligned section of track then damps pre-existing oscillations by a factor >500.

Within this section the bucket must also receive continued acceleration to maintain V_T in spite of electromagnetic drag. The drag force F_D is related to the levitation force F_L and guidance force F_G (Ref. 12):

$$F_D=\left(\frac{8\rho_{guide}}{\pi\mu_0V_Tu}\right)^{\frac{1}{2}}(F_L+F_G) \tag{9}$$

ρ_{guide} is the resistivity of guideway in ohm-meters; u is in Fig. 4b. For an aluminum guideway with $u=25$ cm, $F_D=0.00977$ (F_L+F_G) at the cited V_T. F_L in turn is very nearly the repulsion of a long conductor carrying current i from a parallel surrounding semicylinder of radius S (the guideway); the repulsion is normal to the semicylinder diameter and is approximated as the repulsion between i and an image current $-i$ a distance S below the semicylinder and on its symmetry plane:

$$F_L=K\cdot\mu_0 i^2 l_c/4\pi S \quad \text{N} \qquad F_G=k_2|\bar{X}_2| \quad \text{N} \qquad (10)$$

F_G is associated with mean displacement $\bar{X}_2$ from equilibrium through Eq. (5). K is a geometrical factor of order unity; if the semicylinder were replaced by a flat sheet, K would be unity. With $l_c=2$ m and i, S as before, $F_L=K\cdot 33{,}333$N. Hence the bucket experiences deceleration $dV_T/dt\sim 10$ m/s^2. Since this is two orders of magnitude less than the main acceleration, 1000 m/s^2,[1] the passive damping section serves as well for adjustment of V_T to a desired value.

IV. Separation and Snapout

Following passive damping, it is necessary to separate payload from bucket and to remove the bucket laterally so as to permit its regenerative braking. These actions must be accomplished with minimum perturbation to the payload. An approach to this goal is indicated in Fig. 8; this approach relies on bucket accelerations only, with no active mechanisms aboard the bucket. Thus Fig. 8a indicates schematically the sequence of accelerations $\ddot{x}$ applied to the bucket; Fig. 8b shows the resultant payload response, within the mechanism of Fig. 4a. We have:

1) Passive damping acceleration—This is required by Eqs. (9) and (10). The payload remains tightly enclosed within its housing, as in Fig. 4.

2) Wrenchout—During main acceleration the payload will have wedged tightly into its housing. Wrenchout is a sharp deceleration of short duration, which wrenches the payload free and sends it forward within the bucket; this forward motion is damped by the support boom. Forward motion must exceed the payload diameter $2a$.

3) Separation—Closely spaced impulses of bucket acceleration and deceleration translate the bucket forward a distance $\sim a$ with respect to the payload, which then is in free flight.

4) Snapout—The guideway curves away, carrying with it the bucket, which is snapped away from the payload flight path. Figure 8c illustrates this motion.

It has been proposed[1] that the bucket magnetic field acting on the payload during snapout could yield $\Delta V_Z=4$ cm/s. This perturbation results from the payload being strongly paramagnetic and from its containing fine-grained metallic iron as well. Metallic Fe typically comprises 0.5-0.6% by weight of lunar soils, of which 0.15-0.2% is in the form of fragments >0.01 cm across. The remainder is finer grained and much of it is superparamagnetic. Mare fines also contain typically 15-20% of the strongly paramagnetic FeO.[13]

We use the unrationalized cgs electromagnetic system of units when considering rock magnetism. Thus a reference payload of mass 2×10^4 g has specific susceptibility $\chi_S=2.4\times 10^{-3}$ (G-cm^3)/(Oe-g),[14] where 1 Oe (oersted) $=10^{-4}$ T (tesla). Within the payload, 0.2% is iron, having specific magnetization $\sigma_S=220$ G-cm^3/g. We introduce three assumptions: 1) the payload behaves magnetically as a point dipole. (In any case one may separate the free iron and form it into a compact payload core.) 2) The iron core may always be regarded as saturated magnetically. (Soft iron may reach >70% of saturation for $H<10$ Oe.) 3) Hysteresis in the iron is negligible.

We regard the payload motion during snapout as lying on the z axis of Fig. 4b. The Biot-Savart law then gives the magnitude H of the bucket magnetic field:

$$H=\frac{\mu_0 izu}{\pi}\left(\frac{(z^2+5u^2)^{-1/2}}{z^2+4u^2}-\frac{(z^2+17u^2)^{-1/2}}{z^2+16u^2}\right) \quad \text{Oe} \qquad (11)$$

and the payload motion is given by $z=z(t)$. Here H results from conductors 1-4 only. Also $H>0$ for all z, and $H=H(z)$ has a single maximum. The resulting ΔV_Z on the payload is given:

$$(\Delta V_Z)_{para}=\chi_S\int_t \frac{\partial H}{\partial z}H dt \ \text{cm/s}$$
$$(\Delta V_Z)_{Fe}=\alpha\sigma_S\int_t \frac{\partial H}{\partial t}dt \ \text{cm/s} \qquad (12)$$

due respectively to paramagnetism and ferromagnetism; α is the mass fraction of iron. It now is possible to define a reference snapout maneuver, characterized by a maximum $\ddot{z}$. This maneuver involves four stages:

1) Pullout—The guideway curves away so as to produce $\ddot{z}=\ddot{z}_a$. This continues to the point $H=H_{max}$, e.g., to the value of z which maximizes H. At that point $\dot{z}=\dot{z}_{max}$ and is maximized; for the payload, ΔV_Z then is maximized also.

2) Pullin—The guideway curves in the opposite direction, producing $\ddot{z}=-\ddot{z}_{max}$. This continues to the point $\partial H/\partial z=(\partial H/\partial z)_{min}<0$, at which we require $\dot{z}=0$. In general $\ddot{z}_{max}\neq\ddot{z}_a$ since it is necessary to limit $\dot{z}_{max}$ so as to achieve $\dot{z}=0$ at the cited point.

3) Cruise—At $\partial H/\partial z=(\partial H/\partial z)_{min}$ with $\dot{z}=\ddot{z}=0$. This stage may be introduced to drive ΔV_Z to zero.

4) Cutoff—The bucket passes under a magnetic shield of soft iron or mu-metal.

In Eq. (11), with $u=25$ cm, $H_{max}=114.147$ Oe at $z=32.91$ cm; $(\partial H/\partial z)_{min}=-1.5715$ Oe/cm at $z=57.69$ cm, at which $H=86.574$ Oe. With χ_S, σ_S, α as given, we arbitrarily choose $\ddot{z}_{max}=630$ m/s^2, close to the maximum allowed by the clearance (2 cm) between bucket thermal shield and guideway in Fig. 4. The snapout then proceeds:

1) Pullout

$$\ddot{z}_a=474.4 \text{ m/s}^2 \qquad 0\le t\le 0.03725\text{s}$$
$$\dot{z}_{max}=17.671 \text{ m/s} \quad \text{at} \quad z=32.91 \text{ cm}$$
$$(\Delta V_Z)_{para}=1.4702\times 10^{-2} \text{ cm/s}$$
$$(\Delta V_Z)_{Fe}=7.0695\times 10^{-2} \text{ cm/s}$$

2) Pullin

$$\ddot{z}=-630 \text{ m/s}^2 \qquad 0.03725\le t\le 0.0653\text{s}$$
$$\dot{z}=0 \quad \text{at} \quad z=57.69 \text{ cm}$$
$$(\Delta V_Z)_{para}=0.6234\times 10^{-2} \text{ cm/s}$$
$$(\Delta V_Z)_{Fe}=5.4043\times 10^{-2} \text{ cm/s}$$

3) Cruise

$$d(\Delta V_Z)_{para}/dt=-0.32652 \text{ cm/s}^2$$
$$d(\Delta V_Z)_{Fe}/dt=-0.69146 \text{ cm/s}^2$$

Hence $\Delta V_Z=0$ at $t=0.1245$ s.

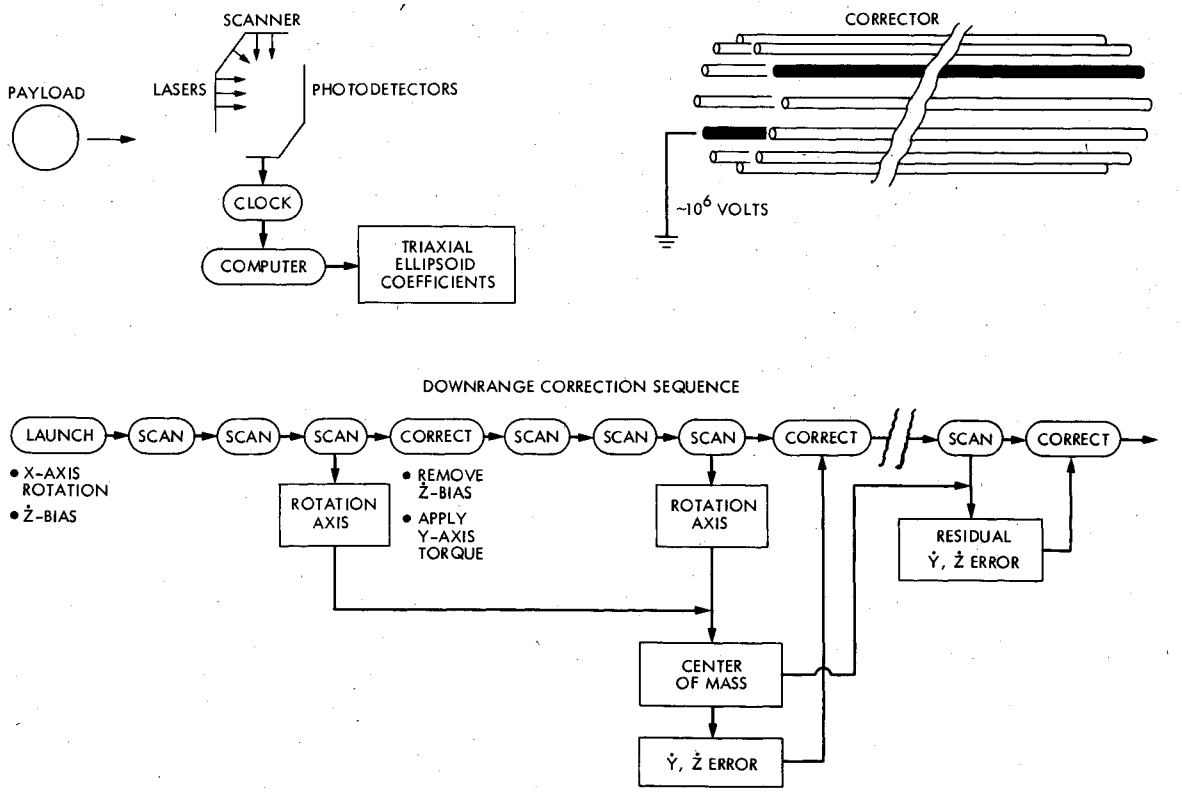

Fig. 9 Downrange tracking and correction: a) optical scanner; b) electrostatic transverse corrector; c) sequence of scanning and correction, with information flow.

The cruise phase is optional; it is included here to show that so far from introducing $\Delta V_Z = 4$ cm/s during snapout, one may arrange $\Delta V_Z = 0$. With the cruise deleted, snapout at 2400 m/s requires 156.72 m of guideway and produces $\Delta V_Z = 0.0603$ cm/s.

V. Downrange Correction

Downrange correction involves repeated optical scanning and position determination of a payload in flight, followed by adjustment of its velocity components (Fig. 9). The scanning is performed with an array of lasers incident upon photodetectors, which are occulted by the payload passage. Thus let the payload be a triaxial ellipsoid:

$$Ax^2 + By^2 + Cz^2 + 2Dxy + 2Exz + 2Fyz + Gx + Hy + Iz - 1 = 0 \tag{13}$$

By appropriately timing the occultations one obtains data from which A, B, ..., I are found; these coefficients then determine both payload orientation in space, and location in space of the center of figure (CF).

Figure 9 then illustrates a sequence for downrange correction. Initially the payload requires a rotation $\omega_x \sim 0.1$ rad/s about the x axis (in direction of motion); this is imposed by a screw twist in the guideway during the separation sequence of Fig. 8a, b. Also, the velocity vector post-snapout is regarded as biased by $(\Delta V_Z)_b = 6$ cm/s, which is to be removed.

Initially the payload in flight is optically scanned three times in succession, the scanners being some 1 km apart. Under Chasles' theorem, the resulting data discriminate between effects due to spin ω_x and to lateral motion of the CF. One then determines the true orientation of the spin axis, which in general will have been perturbed during release.

Next, one applies transverse correction in the z direction to remove $(\Delta V_Z)_b$. The correcting force acts as if applied at the CF, but the CF is displaced from the center of mass (CM) by distance d. Hence removal of $(\Delta V_Z)_b$ torques the payload about the y axis and introduces a rotation component $\omega_y = 5(\Delta V_Z)_b d/(A^{-1} + C^{-1})$, the payload being regarded as a uniformly dense ellipsoid having moment of inertia $m_p(A^{-1} + C^{-1})/5$ about the y axis, where m_p is its mass. For a nearly spherical payload of $a \sim A^{1/2} \sim C^{-1/2} = 13$ cm and $d = 10$ cm, $\omega_y \sim 0.1$ rad/s. There is then a new spin vector $\omega = \omega_x \hat{i} + \omega_y \hat{j}$, and a new orientation of the spin axis.

One then scans again three times in succession, and locates this new spin axis. The intersection of the new and old spin axes determines the payload CM. Now it is possible to call up the earlier data on payload position, and to interpret them in terms of true lateral motion of the CM; e.g., of components ΔV_N, ΔV_Z. These are then corrected.

Finally, one allows the payload to fly past a mountain located as far as possible downrange, thus allowing residual errors ΔV_N, ΔV_Z to integrate into displacements. One detects these displacements with a final scan, and removes the residual ΔV_N, ΔV_Z with a terminal correction at the mountain.

Figure 10 then defines the available accuracy; this lunar photograph shows the terrain available for emplacement of a mass-driver system which launches to the vicinity of L_2.[4] Point 1 is the theoretical optimum, on the equator at 33.1°E longitude, but is located in unfavorably rugged terrain. Points 2 and 3 are in favorably flat mare terrain. Point 3 has the additional advantage that, respectively, 57 and 71 km downrange are mountain peaks (points 4 and 5), which may be well-suited as locations for terminal scanning and correction. If the CM can be located to give a position error accurate to ±0.1 cm,§ then with flight time (integration time) of 30 s between points 1 and 5, following all corrections one has a residual $\Delta V_N = \pm 0.003$ cm/s. From Fig. 1, the resultant miss at L_2 is ±1.5 m.

§Laser beams can be focused more tightly, but one seeks occultation data descriptive of an overall payload shape and not of local roughnesses in its surface.

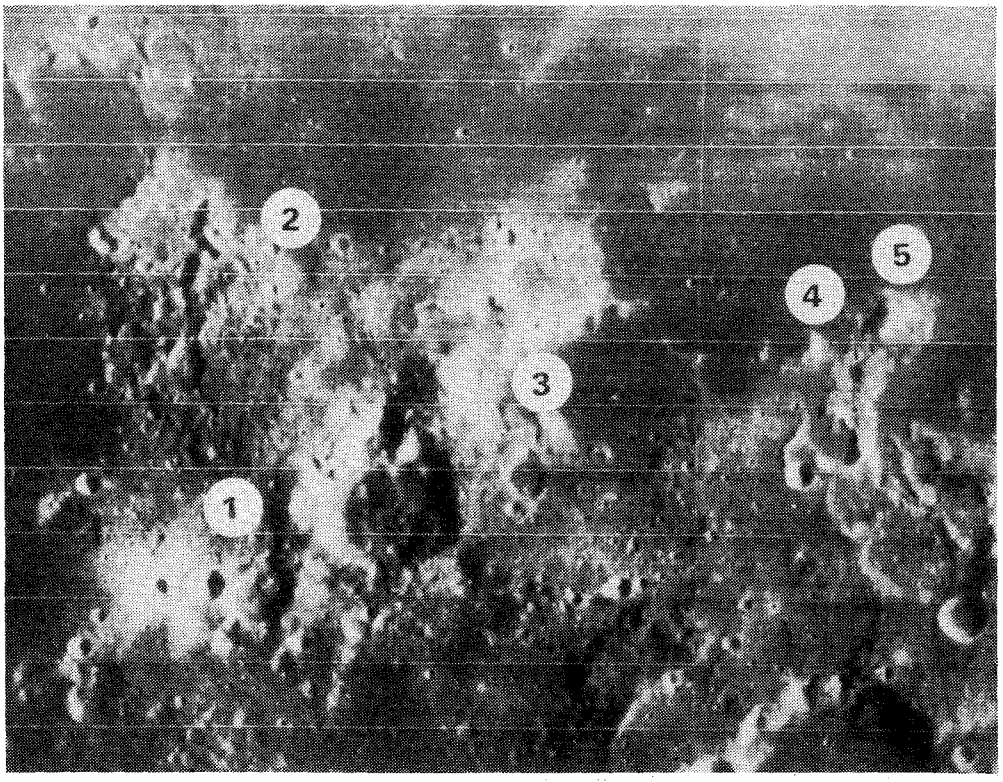

Fig. 10 Medium-resolution photography of the lunar launch range (see text for identification of points). Mare Tranquillitatis is to the north (top). [From Lunar Orbiter photo IV 73 H_1; scale = 1:1,400,000 (1 mm = 1.4 km)].

Consider further the functions of scanning and correction. Figure 11 presents three-view drawings of an array of six numbered lasers capable of determining the coefficients of Eq. (13). Payload motion is along the x axis. With timing initiated prior to occultation, the ith laser beam shows time t_{i1} of being occulted by the payload, and time t_{i2} of emergence from occultation. The associated x values are $x_{i1} = V_T t_{i1}$, $x_{i2} = V_T t_{i2}$. Hence, from Eq. (13), we have:

Determination of A, G—From laser 1 at $y = 0$,

$$Ax_{11}^2 + Gx_{11} - 1 = 0 \qquad Ax_{12}^2 + Gx_{12} - 1 = 0 \tag{14}$$

Determination of D—From laser 2 at $y = y_2$,

$$\begin{aligned} Ax_{21}^2 + By_2^2 + 2Dx_{21}y_2 + Gx_{21} + Hy_2 - 1 = 0 \\ Ax_{22}^2 + By_2^2 + 2Dx_{22}y_2 + Gx_{22} + Hy_2 - 1 = 0 \end{aligned} \tag{15}$$

Determination of B, H—From laser 3 at $y = y_3$,

$$\begin{aligned} Ax_{31}^2 + By_3^2 + 2Dx_{31}y_3 + Gx_{31} + Hy_3 - 1 = 0 \\ Ax_{32}^2 + By_3^2 + 2Dx_{32}y_3 + Gx_{32} + Hy_3 - 1 = 0 \end{aligned} \tag{16}$$

and B, H are found from either of Eqs. (15) with either of Eqs. (16).

Determination of E, C, I—From lasers 4 and 5, respectively, at $z = z_4$, z_5, as D, B, H are found via lasers 2 and 3.

Determination of F—Laser 6 is at (x_6, y_6, z_6) and its beam defines the line, $x - x_6 = y_6 - y = z - z_6$. Hence knowledge of t_{61} defines $(x = x_{61}, y = y_{61}, z = z_{61})$ and similarly for t_{62}; then Eq. (13) involves only the single unknown F.

Velocity correction can also be achieved magnetically via the principles of Sec. IV, with the payload having magnetic properties as noted. Thus Fig. 12a is a cross section of a magnetic transverse corrector analogous to the electrostatic corrector of Fig. 9; payload motion is normal to the plane of the page. The corrector is a cylindrical array of radially oriented bifilar lines. Each bifilar line is a pair of linear conductors of length l_s (the sector length), radius r, separated by distance $d \ll l_s$; any one such bifilar line may be driven by being made to carry current i. Figure 12b shows such a driven bifilar line, with the payload passing parallel to its length and with its center at distance y from the nearer conductor. The magnetic field at y and its derivative are given:

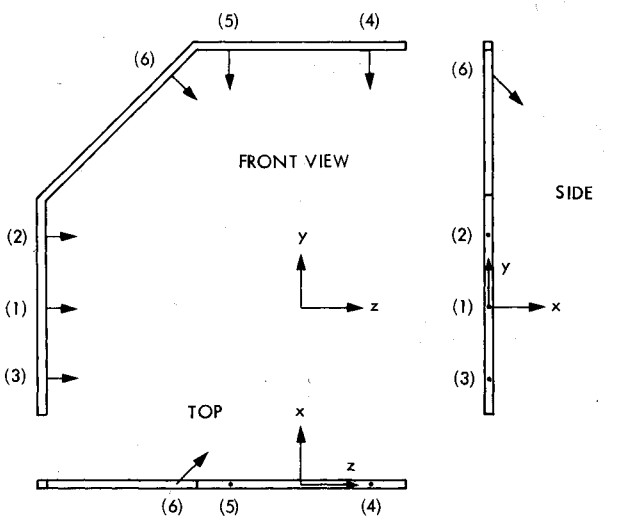

Fig. 11 Three-view representation of arrangement of lasers in the optical scanner of Fig. 9.

$$H = (\mu_0 i/2\pi)\,[1/y - 1/(y+d)] \quad \text{Oe}$$

$$\frac{dH}{dy} = -(\mu_0 i/2\pi)\,[1/y^2 - 1(y+d)^2] \quad \text{Oe/cm} \tag{17}$$

The inductance of the bifilar line is[15]

$$L = (\mu_0 l_s/\pi)\,[1 + 4\,\ell n(d/r)] \quad \text{H} \tag{18}$$

and the energy in the system is $\frac{1}{2}Li^2$. This energy is to be fed from a capacitor; the system then behaves as an LC circuit closely analogous to the drive circuits of the mass-driver itself. To illustrate this, consider a system as in Fig. 12 adapted from the specifications of the mass-driver of Fig. 4 (Ref. 1): $L=13.17$ μH, $i_{max}=77{,}447$ A, $l_s=20$ m, $C=337.4$ μF, $V_{max}=15{,}300$ V, and $r=2$ cm. We replace L by $2L$; then $d=42$ cm, a reasonable value. Hence to maintain V_{max} we also replace C by $2C$; system energy then is 79,000 J. Taking $y=15$ cm, and determining $\ddot{y}$ via Eqs. (12) and (17) with $\alpha=0.002$, $(\ddot{y}_{para})_{max}=117$ cm/s^2 and $(\ddot{y}_{Fe})_{max}=28.2$ cm/s^2, associated with i_{max}. Also the average value is $\bar{\ddot{y}}=(2/\pi)\ddot{y}_{max}$ so each sector produces $\Delta\dot{y}=0.77$ cm/s, for $V_T=2400$ m/s. We have $(2L\cdot 2C)^{-\frac{1}{2}}=7500$ s^{-1} giving 20 half-wave oscillations in i per sector. The polarity of σ_S follows that of i (and dH/dy); hence the system behaves as a rectified LC circuit, having the behavior of Fig. 12c. Each half-wave oscillation of force F produces $\Delta\dot{y}=0.0385$ cm/s.

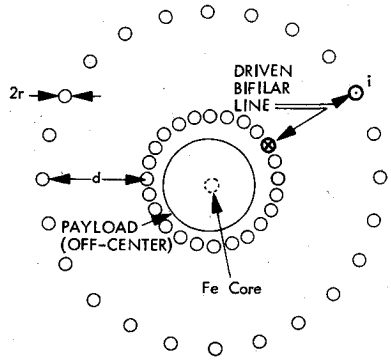

Fig. 12a Cross section of magnetic transverse corrector with payload.

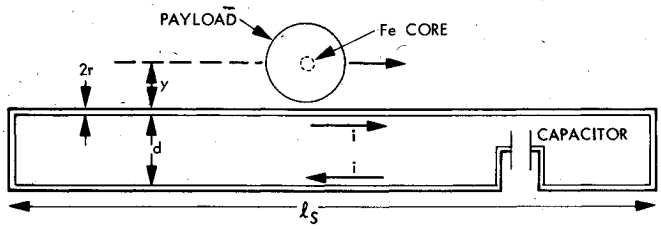

Fig. 12b Plan view of driven bifilar line with payload.

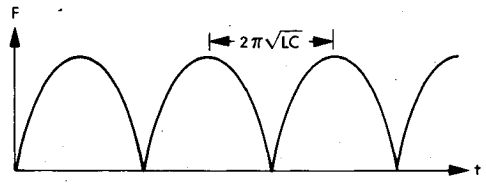

Fig. 12c Resulting curve of force on payload vs time.

It is possible to adjust V_T for a payload in flight. In Fig. 13 an array of tandem rings are connected by circuit breakers to a capacitor, each in turn generating the field of a ring current i. The rings are of radius R; their mutual separation is Δx. At a distance x from the ring plane and at distance ρ off-axis, the magnetic field H has components H_x, H_ρ:

$$H_x=\frac{\mu_0 i}{2\pi}\frac{x}{\rho[(R+\rho)^2+x^2]^{\frac{1}{2}}}\left(\frac{R^2+\rho^2+x^2}{(R-\rho)^2+x^2}E(k)-K(k)\right)$$

$$H_\rho=\frac{\mu_0 i}{2\pi}\frac{1}{[(R+\rho)^2+x^2]^{\frac{1}{2}}}\left(\frac{R^2-\rho^2-x^2}{(R-\rho)^2+x^2}E(k)+K(k)\right) \tag{19}$$

where $K(k)$ and $E(k)$ are the complete elliptic integrals of the first and second kind, respectively, and k is the modulus

$$k^2=4R\rho/[(R+\rho)^2+x^2]$$

For $\rho \ll R$,

$$H_x=\frac{\mu_0 iR^2}{2(R^2+x^2)^{3/2}}+O(\rho^2)\quad H_\rho=\frac{3}{4}\frac{\mu_0 ixR^2\rho}{(R^2+x^2)^{5/2}}+O(\rho^2) \tag{20}$$

The payload has specific magnetization

$$M_S=M_S H/(H\cdot H)^{\frac{1}{2}}$$

The payload acceleration then is $\Delta\dot{V}=\nabla(M_S\cdot H)$; in cylindrical coordinates, the gradient operator ∇ is

$$\nabla=\frac{\partial}{\partial\rho}\hat{\rho}+\frac{1}{\rho}\frac{\partial}{\partial\theta}\hat{\theta}+\frac{\partial}{\partial x}\hat{x} \tag{21}$$

where (ρ,θ,x) are coordinates; $(\hat{\rho},\hat{\theta},\hat{x})$ their associated unit vectors. Hence

$$\Delta\dot{V}=\Delta\dot{\rho}\hat{\rho}+\Delta\dot{V}_T\hat{x}=\frac{3}{2}M_S\frac{\mu_0 iR^2x}{(R^2+x^2)^{5/2}}\left(\frac{1}{2}\hat{\rho}-\hat{x}\right)\ \text{cm/s}^2 \tag{22}$$

so the payload is accelerated away from the centerline and gains transverse velocity $\Delta\dot{\rho}=\frac{1}{2}\Delta V_T$. Hence it is necessary to operate longitudinal and transverse magnetic correctors in tandem, first obtaining a desired ΔV_T, then removing the unwanted $\Delta\dot{\rho}$.

Let the arrangement of Fig. 13 function as an LC circuit tuned to the payload motion: $i=i_0\sin\omega t$, $\omega=\pi V_T/\Delta x$. From Eq. (22) the ΔV_T per ring is

$$\Delta V_T=\frac{3}{2}\frac{\bar{M}_S\mu_0 i_0}{V_T R}\int_0^{\Delta x}\frac{R}{\Delta x}\frac{(x/R)\sin(\pi x/\Delta x)}{(1+x^2/R^2)^{5/2}}\,d(x/R)\quad\frac{\text{cm/s}}{\text{ring}} \tag{23}$$

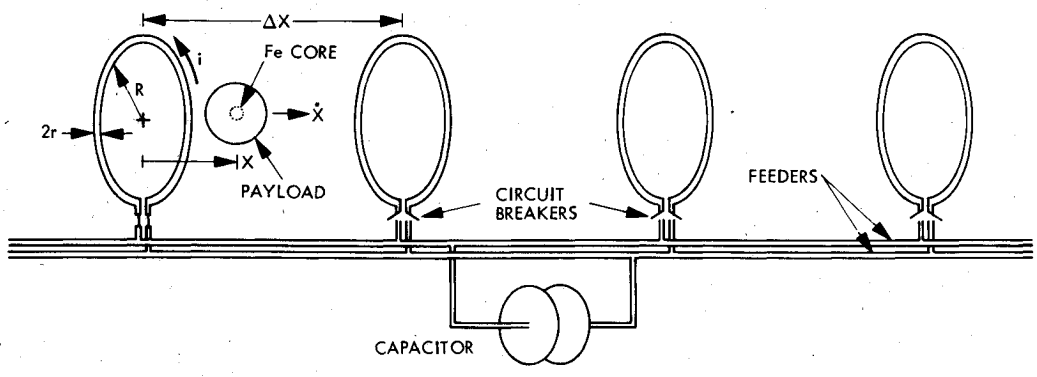

Fig. 13 Ring-type magnetic corrector for V_T.

where $\bar{M}_S$ is the mean value of M_S. To maximize $\Delta V_T = \Delta V_T(\Delta x)$, there is the theorem,

$$\frac{\mathrm{d}}{\mathrm{d}a}\int_0^a f(x,a)\,\mathrm{d}x = f(a,a) + \int_0^a \frac{\partial}{\partial a} f(x,a)\,\mathrm{d}x \tag{24}$$

Hence ΔV_T is maximized for $\Delta x/R = 0.936187$ and for this value the definite integral of Eq. (23) has the value 0.155408. Also $\bar{M}_S$ involves contributions from both ferromagnetism and paramagnetism; from Eq. (20),

$$\bar{M}_S = \alpha\sigma_S + \frac{\chi_S}{\pi}\frac{\mu_0 i_0}{2R}\int_0^l \frac{\sin(\pi x/\Delta x)}{(1+x^2/R^2)^{3/2}}\,\mathrm{d}\left(\frac{x}{\Delta x}\right) \text{ G-cm}^3/\text{g} \tag{25}$$

where the definite integral gives the mean value $\bar{H}_x$, and again the payload magnetism is regarded as that of a point dipole. In Eq. (25) with the cited $\Delta x/R$, the value of the definite integral is 1.473083. Then, taking $\alpha = 0.002$, $\sigma_S = 220$, $\chi_S = 2.4\times10^{-3}$ as before, and with $i_0 = 77{,}447$ A, $R = 15$ cm, $\Delta V_T = 2.578\times10^{-2}$ cm/s per ring. With a 20-m length of rings, $\Delta V_T = 3.6716$ cm/s.

The self-inductance of each ring is[15]

$$L = \mu_0[R\ell_n(8R/r-2) + \tfrac{1}{4}] \text{ H} \tag{26}$$

where r is the radius of ring conductor. For $r = 2$ cm with R as given, $L = 1.08$ μH. With $\Delta x = 14.0428$ cm, the tuned LC system frequency is $(LC)^{1/2} = 53{,}691.7$ s^{-1}; hence $C = 321.3$ μF. The energy is $\frac{1}{2}Li_0^2 = 3237.5$ J and hence peak voltage is $V_{\max} = 4489$ V.

VI. In-Flight Payload Perturbations

The attainment of a circular error probable at L_2 of 3 m, as proposed here, is not vitiated by payload perturbations while in flight. The most important perturbation is due to solar radiation pressure.[16] For a flight time of 44.5 h,[4] two payloads of 13-cm radius and 20-kg mass experience a relative dispersion of 1.54 m per difference of 0.01 in mean albedo, for a solar constant of 1360 W/m^2.[17] Small albedo differences are particularly easy to control when the payload is of low albedo. A 3% variation in mass has the same effect as a variation of 0.01 in mean albedo. Hence the quality control of payload uniformity need not be exceptional to ensure that the largest source of target dispersion is the residual ΔV_N remaining following the correction sequence of Fig. 9.

VII. Conclusions

We have proposed a number of new concepts to aid in implementing the concept of a lunar mass-driver system, and have presented analyses which may aid in overcoming some of the problems in precision release and aiming of payloads. We have proposed a payload containment and release system which offers the prospect of payload release with minimal perturbation. This release requires no active mechanism aboard the bucket, but occurs as a passive response to mass-driver accelerations applied to the bucket.

We have introduced "electromagnetic fins" which, with an actively aligned guideway, offer efficient damping of bucket and payload oscillations. We have laid to rest the concern that bucket magnetic fields, acting on a strongly paramagnetic payload during separation of payload from bucket, would be an important source of payload disturbance.

We have proposed a simple optical scanner which determines orientation and position of a triaxially ellipsoidal payload. We have given a sequence of scanning and downrange correction which detects and removes errors in motion of the payload center of mass, to high accuracy. We have discussed magnetic methods for downrange correction, both of transverse and longitudinal velocity errors.

In consideration of the proposed design concepts, of the values of dispersion coefficients, and of available launch range topography, we propose the routine attainment of a circular error probable, for a mass-catcher near the L_2 libration point, of 3 m diam. This conclusion also stands in consideration of solar-radiation perturbations on payloads while in flight.

Acknowledgments

It is a pleasure to acknowledge the support of Stanford University and of its Department of Aeronautics and Astronautics, which provided facilities for the initial part of this research. Other computational and graphics services were provided through the courtesy of the Jet Propulsion Laboratory. We have had valuable discussions with John Breakwell and Jim Stephens. This work represents one phase of research conducted at the Center for Space Science, with support from K.R.G., Inc.

References

[1] Chilton, F., Hibbs, B., Kolm, H., O'Neill, G.K., and Phillips, J., "Mass-Driver Applications," in *Space-Based Manufacturing from Nonterrestrial Materials,* edited by G.K. O'Neill, *Progress in Astronautics and Aeronautics,* Vol. 57, AIAA, New York, 1977, pp. 63-94.

[2] Malzbender, R.M., "Optical Scanning of Mass-Driver Payloads," in *Space Manufacturing Facilities III,* edited by J. Grey, AIAA, New York, 1979, pp. 491-496.

[3] Heppenheimer, T.A., "Two New Propulsion Systems for Use in Space Colonization," *Journal of the British Interplanetary Society,* Vol. 30, Aug. 1977, pp. 301-309.

[4] Heppenheimer, T.A., "Guidance, Trajectory and Capture of Lunar Materials," in *Space Manufacturing Facilities III,* edited by J. Grey, AIAA, New York, 1979, pp. 473-490.

[5] Heppenheimer, T.A., Ross, D.J., and Hannah, E.C., "Electrostatic Velocity Adjustment of Payloads Launched by Lunar Mass-Driver," *Journal of Guidance, Control and Dynamics,* Vol. 5, March-April 1982, pp. 200-209

[6] Chilton, F., Hibbs, B., Kolm, H., O'Neill, G.K., and Phillips, J., "Electromagnetic Mass-Drivers," in *Space-Based Manufacturing from Nonterrestrial Materials,* edited by G.K. O'Neill, *Progress in Astronautics and Aeronautics,* Vol. 57, AIAA, New York, pp. 37-61.

[7] Arnold, W.H., et al., "Dynamics and Design of Electromagnetic Mass-Drivers," in *Space Resources and Space Settlements,* edited by J. Billingham, W. Gilbreath, and B. O'Leary, NASA SP-428, 1979, pp. 85-157.

[8] O'Neill, G.K. and Snow, W.R., "Overview and Outline of Mass-Driver Two," in *Space Manufacturing Facilities III,* edited by J. Grey, AIAA, New York, 1979, pp. 103-107.

[9] Kolm, H.H., Thornton, R.D., Iwasa, Y., and Brown, W.S., "The Magneplane System," *Cryogenics,* Vol. 15, July 1975, pp. 981-995.

[10] Connell, D., et al., "Support and Alignment," *The Stanford Two-Mile Accelerator,* edited by R.B. Neal, W.A. Benjamin Co., Reading, Mass., 1968, Chap. 22, pp. 821-866.

[11] Hulm, J.K. and Matthias, B.T., "High-Field, High-Current Superconductors," *Science,* Vol. 208, May 23, 1980, pp. 881-887.

[12] Borcherts, R.H., Davis, L.C., Reitz, J.R., and Wilkie, D.F., "Baseline Specifications for a Magnetically-Suspended High-Speed Vehicle," *Proceedings of the IEEE,* Vol. 61, May 1973, pp. 569-578.

[13] Phinney, W.C., Criswell, D., Drexler, E., and Garmirian, J., "Lunar Resources and Their Utilization," in *Space-Based Manufacturing from Nonterrestrial Materials,* edited by G.K. O'Neill, *Progress in Astronautics and Aeronautics,* Vol. 57, AIAA, New York, pp. 97-123.

[14] Runcorn, S.K., Collinson, D.W., O'Reilly, W., Stephenson, A., Greenwood, N.N., and Battey, M.H., "Magnetic Properties of Lunar Samples," *Science,* Vol. 167, Jan. 30, 1970, pp. 697-699.

[15] Smythe, W.R., *Static and Dynamic Electricity,* 3rd Ed., McGraw-Hill, New York, 1968, pp. 296-297, 339-342, 290-291.

[16] Von Herzen, B.P., "Light Pressure and Solar Wind Perturbations to Payload Trajectories," in *Space Manufacturing Facilities III,* edited by J. Grey, AIAA, New York, pp. 499-501.

[17] Allen, C.W., *Astrophysical Quantities,* 3rd Ed., Athlone Press, London, 1976, p. 169.